

Preparation of nanoparticles of oxides by the citrate—nitrate process

Effect of metal ions on the thermal decomposition characteristics

S. Banerjee · A. Kumar · P. Sujatha Devi

CTAS2010 Conference Special Chapter
© Akadémiai Kiadó, Budapest, Hungary 2011

Abstract This paper reports preparation of nanoparticles of oxides by the citrate–nitrate process and the effect of metal ions on the thermal decomposition characteristics of the corresponding citrate–nitrate gel precursors. In order to understand the effect of metal ions on the thermal decomposition characteristics of the precursors, we have prepared a series of single component oxides such as MO, where M = Zn, MO₂, where M = Sn, Ce, Zr, and M₂O₃ where M = Al, Fe, Bi. In all the cases the citrate to nitrate ratio was fixed at 0.3. In order to ascertain the decomposition characteristics of the gel samples, TG/DTA studies were performed on the dried gel samples. After complete physico-chemical characterization of the precursors and the calcined products, it could be concluded that the nature of decomposition of the precursors depends largely on the nature of the metal ions. Finally, the advantages of the citrate–nitrate process such as its high degree of reproducibility, its potential for large-scale production of nanocrystalline ceramic oxide powders and its lower cost could be established based on a series of experiments and examples.

Keywords Nano-crystalline · Ceramic metal oxides · Citrate–nitrate ratio · Thermal analysis · XRD and TEM analysis

Introduction

In recent years, there is a renewed interest in the preparation of nanoparticles of oxides due to their increasing demand in technological applications. For example, metal oxides such as ZnO, Fe₂O₃, and SnO₂ are well known for their gas sensing applications. Sensors made with such nano-sized metal oxide powders are found to exhibit high sensitivity at low operating temperature towards different gases like ethanol, acetone, LPG, CNG, etc. Alumina, on the other hand, is an advanced ceramic material with unique physical properties with applications ranging from abrasives, refractories, lasers, high alumina cements, toughened ceramics, and substrates for microelectronic computer chips. Due to their high oxide ion conductivity, doped zirconia, ceria, and bismuth oxides are potential materials as solid electrolytes for solid oxide fuel cell applications. Therefore, from the technological point of view, there is an increasing demand to develop processes that could yield nanoparticles of such oxides with superior properties at a lower cost.

Various wet chemical methods [1–19] are available for the preparation of nanoparticles of oxides. Processes such as co-precipitation technique, sol gel technique, hydrothermal synthesis, and micro emulsion process generally involve the use of auxiliary reagents such as acids or bases, templates, surfactants or dispersing agents for either to convert, immobilize or to finely divide the corresponding metal precursors to the corresponding oxides. Besides, various other organic solvent assisted routes such as solvothermal synthesis, sol gel with or without supercritical drying, oil drop methods, template synthesis, etc. and some more sophisticated methods such as flame pyrolysis, arc and plasma discharge, sputtering, microwave irradiation, molten salt flux methods, solid state reactions mechanical

S. Banerjee · A. Kumar · P. Sujatha Devi (✉)
Nano-Structured Materials Division, Central Glass and Ceramic Research Institute, CSIR, Kolkata 700032, India
e-mail: psujathadevi@cgcri.res.in; psujathadevi@gmail.com

A. Kumar
Defence Metallurgical Research Laboratory, Hyderabad 500058,
India

alloying, and inert gas condensation, etc. are also available for the preparation of oxides. Each method has its own merits and demerits. Compared to most of the processing routes mentioned above, combustion process [20–41] is a low cost technique with high degree of reproducibility and a good potential for large-scale production of oxides. Compared to other methods, productivity is high in combustion synthesis since concentrated metal solutions can be used and neither aging nor any washing methods are required which are necessary steps in other processes such as co-precipitation methods. Moreover, high purity powder can be easily obtained that are free of chlorine or any other impurity by proper use of metal precursors. Since, large volume of gases are released during combustion, it limits particle contact and hence coarsening and agglomeration of the powder. Hence, among all the wet chemical processes, the combustion process has recently emerged as a highly promising powder preparation technique mainly due to its simplicity, reproducibility, lower cost of production, ease to upscale and low energy consumption as detailed above. Among the various combustion processes available, glycine–nitrate process (GNP) and citrate–nitrate process (CNP) are the most popular ones. CNP is a much simpler, cheaper and safer process than GNP. Our group has been working on the citrate–nitrate combustion process which was first developed for the low temperature synthesis of phase pure perovskites and superconducting oxides, and later extended for the synthesis and large-scale production of other multi component oxides with diverse properties [30–38]. Recently, we have reported the preparation of nanoparticles of Al_2O_3 and CeO_2 by the CNP wherein the citrate to nitrate ratio (CIT/NIT or C/N) was varied and optimized as 0.3 [36–38]. In this paper, we have compared the thermal decomposition characteristics of the precursor gels of a series of single component oxides such as MO where M = Zn, MO_2 , where M = Sn, Ce, Zr, and M_2O_3 where M = Al, Fe, Bi prepared by the CNP with a fixed C/N ratio of 0.3. This particular C/N ratio was fixed based on our previous results on ceria and alumina. The oxides obtained using this optimized ratio have been characterized by different techniques to highlight the importance of this process.

Materials and experimental methods

All the chemicals used were of analytical reagent grade. In this process, an aqueous solution of 0.2(M) stock solutions of different metals such as Zn, Al, Fe, Bi, Sn, Zr, and Ce were prepared from the corresponding nitrate, chloride or acetate precursors. For the preparation of different batches, calculated amount of citric acid monohydrate ($\text{C}_6\text{H}_8\text{O}_7 \cdot \text{H}_2\text{O}$, 99.5% Merck Ltd, Mumbai, India) was added to each of the

metal salt solutions (0.2 M) according to the metal batch compositions shown in Table 1. A fixed citrate to nitrate ratio of 0.3 has been used in all the cases. The above mixed solution was allowed to evaporate on a hot plate with stirring (hot plate temperature $200 \pm 5^\circ\text{C}$). The homogeneously mixed solution became viscous and turned into a gel during heating. The gel slowly foams, swells, and finally burns on its own, and once ignited at any point, the ignition slowly propagated forward until the whole sample was fully burnt to produce the corresponding ash powder. The auto-ignition was completed within a few seconds, giving rise to a voluminous powder. The mode of decomposition and burning steps were monitored visually. The gels collected were air dried. The ash powders obtained after the combustion were ground in an agate mortar and calcined at various temperatures for 6 h. In Table 1, the different batches of gels with their preparation conditions are tabulated.

Characterization of the precursor gel and the powder samples

The thermal decomposition characteristics of the dried gel precursors were studied by means of differential thermal analysis (DTA) and thermogravimetric analysis (TG) techniques. N_2 was used as the purge gas in these measurements. These studies were carried out from room temperature to 1273 K at a heating rate of 283 K/min on a NETZSCH thermal analyzer unit (409C) using α -alumina as a reference material for DTA. The enthalpy change, ΔH , has been calculated from the area under the peak using an in-built software in the system. The room temperature powder X-ray diffraction (XRD) was carried out both on the combustion synthesized and calcined powders for phase identification using a Philips X-ray diffractometer (PW1730) with $\text{Cu K}\alpha$ radiation at a 2θ scan rate of $2^\circ/\text{min}$. The crystallite size has been calculated from X-ray line broadening using Scherrer formula. Particle size analysis of the calcined powders was carried out using a Sedigraph 5100 Micromeritics particle size analyzer. Surface area of the calcined powder was measured on a Micromeritics Gemini II 2370 surface area analyzer. The specific surface area (SSA) was converted into particle size assuming that the particles are closed spheres with smooth surface and uniform size. D_{BET} is the particle size calculated from the BET surface area measurement assuming that the particles are having spherical or nearly spherical shape from the equation, $D_{\text{BET}} = 6 \times 10^3 / d_{\text{th}} S_{\text{BET}}$, where d_{th} is the theoretical density of the material under consideration, D_{BET} is the average particle size in nm and S_{BET} is the specific surface area expressed in $\text{m}^2 \text{ g}^{-1}$. Micro structural studies on the powder samples were carried out on a Leo 430i Scanning electron microscope. Particle size and powder

Table 1 Preparation conditions and the nature of decomposition of the different gel precursors

ID	Sample nos.	Nature of decomposition	C_{GEL}	T_{ASH}	C_{ASH}
C1	CeO_2	Moderate decomposition with glowing flints	Light yellow	Fine, fluffy and porous	Off-white
F1	Fe_2O_3	Rapid decomposition with glowing flints	Brown	Fine	Brown
A1	Al_2O_3	Rapid decomposition, no glowing flints	Yellow	Fine	Yellow
B1	Bi_2O_3	Slow decomposition with glowing flints and flame	Yellowish white	Coarse	Ash green
Zr1	ZrO_2	Rapid decomposition with controlled burning and glowing flints	White	Fine	Light brown
Sn1	SnO_2	Sluggish decomposition with glowing flints and flame	White, transparent	Fine and porous	Black
Zn1	ZnO	Controlled burning with rapid decomposition and glowing flints	White, transparent	Fine, fluffy and porous	Light pink/cream

C_{GEL} color of the decomposed gel precursor, C_{ASH} color of the decomposed ash powder, T_{ASH} texture of the ash powder

morphology of the synthesized powders were further monitored with the help of a transmission electron microscope (TEM), JEOL (JEM-200X).

Results and discussion

General characteristics

All the gel samples were hygroscopic, viscous, and sticky in nature and exhibited different colors depending on the nature of the metal cations. The conditions employed for preparing different batches and their physical characteristics are given in Table 1. The gel compositions are designated with a “g” after the sample identification. The color of the uncalcined powder samples also varied with the metal cations. The powder samples derived from the gels Zn1g, Zr1g, and Sn1g were white in color, A1g, C1g, and B1g were yellow and F1g was brown in color. The ash and the calcined powder samples will henceforth be designated as M1U and M1C where M = corresponding metal ion, U = uncalcined, C = calcined, respectively, in the text and in the figures.

TG and DTA studies on gel samples

The thermal decomposition behavior of the dried gels was found to depend strongly on the nature of the starting metal nitrate solutions. Figures 1, 2, and 3 illustrate the simultaneous TG/DTA curves of few representative gel samples. Although the fixed C/N ratio of 0.3 has been used in all the cases, the different metal oxide gel precursors exhibited different thermal decomposition characteristics. Depending upon the nature of the metal cation, the decomposition behavior of the gels could be classified into two distinct categories.

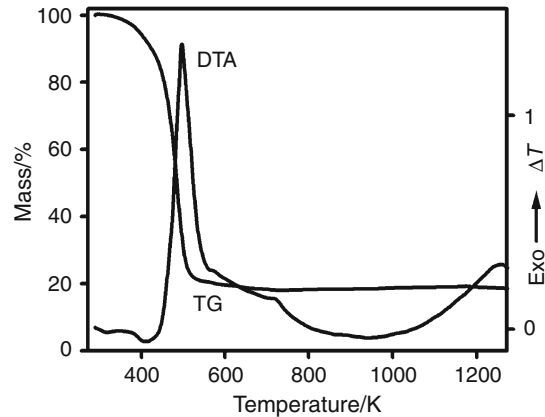


Fig. 1 TG/DTA graphs of Zn1 gel sample indicating a single step decomposition behavior

Single step decomposition reactions

Among the various gel samples investigated, the gel samples of ceria (C1g) and zinc (Zn1g) exhibited a single step decomposition reaction. In Fig. 1, the thermal analysis graphs obtained for the yellow colored Zn1g dried gel sample is shown as a representative. The Zn1g gel exhibited a weight loss of around 82%, whereas the C1g gel exhibited a higher weight loss of around 95% (figure not shown). These gel samples practically undergo a single step decomposition behavior which occurs at a temperature of 400–500 K as indicated by the very sharp and intense DTA peaks seen in Fig. 1. This is in contrast to a multi-step decomposition behavior normally observed for the amorphous citrate gels decomposition [42, 43]. The onset of this decomposition process starts around 400–423 K and due to the highly exothermic nature of this combustion process, the temperature of the system (Zn1g) increased to 497 K as noted from the corresponding DTA peak temperature. The abrupt fall in weight between 23 K and 500 K for Zn and

Fig. 2 TG and DTA graphs of **a** F1, **b** Zr1, and **c** B1g gel samples indicating their multi-step decomposition behavior

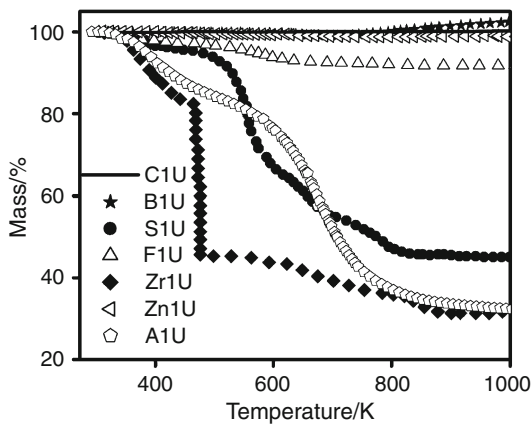
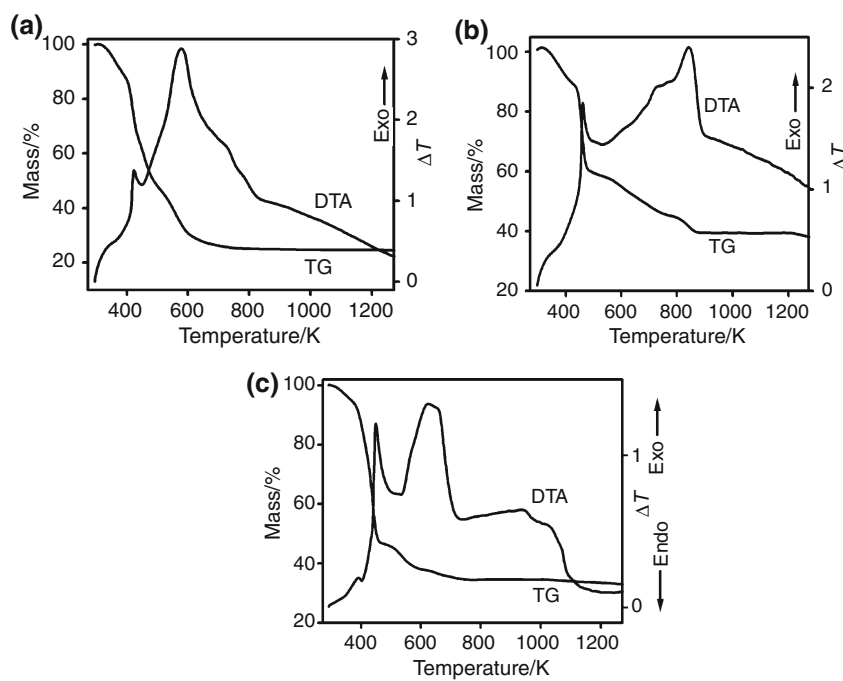


Fig. 3 TG plots of the ash powders of different metal oxide precursors

between 423 K and 534 K for Ce is a further evidence for the single step decomposition nature of the gel during the combustion process. As has been reported earlier, this auto-combustion occurs due to a highly exothermic anionic oxidation-reduction reaction between the nitrate and citrate ions releasing a large amount of gases [30–38, 44–50]. The thermal characteristics associated with the decomposition of the gel samples are tabulated in Table 2.

Multistep decomposition reactions

The decomposition of the gels Sn1g, F1g, Zr1g, A1g, and B1g occurs by a multistep reaction. The representative thermal decomposition graphs of F1g, Zr1g, and B1g gels are shown in Fig. 2a–c, respectively. It is evident from the

TG curves that the weight loss occurs in three definite steps. The DTA peaks of F1g and Zr1g at first showed one small endothermic peak around 350 and 360 K corresponding to weight losses of 10.6 and 10.8% occurring at 296–390 K and 296–424 K as can be seen from their corresponding TG curves. This is followed by two pronounced exothermic peaks as evident from the DTA peaks of F1g and Zr1g gels, first peak around 423 K for F1g and 460 K for Zr1g corresponding to weight losses of 33.0 and 28.64%, respectively, occurring around 395–463 K and 430–485 K, respectively. The second peak around 577 and 843 K corresponding to weight losses of 29.0 and 20.5% occurring in the temperature ranges of 480–611 K and 490–870 K for F1g and Zr1g, respectively. The first endothermic reaction is due to the dehydration of bound water to the metal–citrate complex and the following exothermic reactions are attributed to the decomposition of the gel and oxidation of the corresponding metal–citrate complexes. The decomposition of both the gels appears to complete within 800 K. In the case of B1g, the first and the major decomposition reaction appear to be a single step reaction starting around 448 K with a weight loss of about 53% between 296 and 458 K. This strong exothermic reaction is followed by another exothermic reaction occurring around 617 K as evident from the DTA peak temperature (Fig. 2c). The TG curves also indicate that in addition to the first decomposition step, a relatively small second decomposition also occurs between 500 and 700 K in case of B1g. The formation of a stable intermediate product prior to second step decomposition is indicated by a thermally stable plateau in their TG curves around 450 K.

Table 2 Thermal decomposition characteristics of the different gel precursors prepared by CNP process

Samples	CIT/NIT or F/N	O/R	Valency of the metal ions	W_{loss} (Gel)%	W_{change} (Ash)%	D_T/K	$-\Delta H/\text{J g}^{-1}$
ZnO	0.3	0.926	+2	81	-2.56	497	276
Fe ₂ O ₃	0.3	0.926	+3	75	-8.66	423	140
Al ₂ O ₃	0.3	0.926	+3	77	-70.1	435	436
Bi ₂ O ₃	0.3	0.926	+3	67	+5.34	449	348
ZrO ₂	0.3	0.926	+4	63	-67.8	461	203
SnO ₂	0.3	0.926	+4	91	-39.97	503	322
CeO ₂	0.3	0.74	+4	95	+0.55	533	146

CIT/NIT citrate/nitrate ratio, F/N fuel/nitrate ratio, O/R oxidant/reductant ratio, D_T decomposition temperature, W_{loss} weight loss, ΔH enthalpy changes of the corresponding decomposition reaction

Table 3 Standard enthalpy of formation of oxides

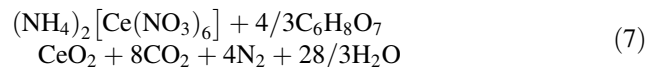
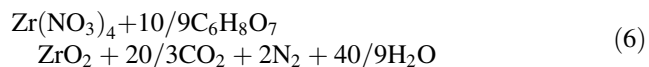
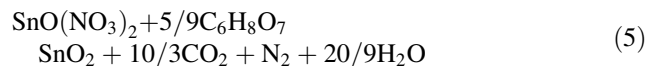
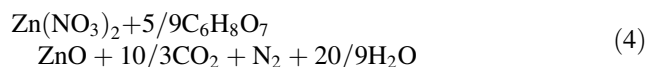
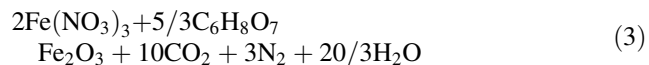
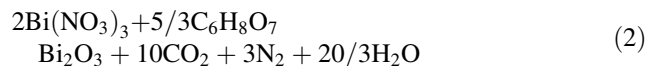
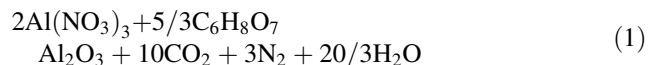
Samples	Standard enthalpy of formation $-\Delta H_f/\text{kJ mol}^{-1}$ $M + O_2 = MO_2$
Al ₂ O ₃	1676
Fe ₂ O ₃	824
SnO ₂	286
ZnO	348
CeO ₂	1089
ZrO ₂	1100
Bi ₂ O ₃	574

Both the DTA peaks showed two pronounced exothermic peaks around 435–450 and 600–800 K, the former indicating the decomposition of the citrate while the latter corresponds to the burning of the residual organic matter and subsequent crystallization of the corresponding metal oxides. The TG curve reveals that the decomposition of the gel appears to be complete within 700 K in case of B1g. The nature of decomposition of the studied gel samples are described in Table 1. The thermal properties associated with the exothermic decomposition of the different gel precursor samples are tabulated in Table 2. The calculated enthalpy change, $-\Delta H$, varied in the order Fe < Ce < Zr < Zn < Sn < Bi < Al with Fe having the smallest enthalpy change and Al exhibiting the highest enthalpy change though all are prepared with a C/N ratio of 0.3. We calculated the standard enthalpies of formation [$-(\Delta H_f)$] of different oxides based on the reaction (e.g., $M + O_2 = MO_2$), given in Table 3 [51]. It is clear that the formation of the oxides from the corresponding metal and oxygen involves a much higher energy change.

The exothermicity of a combustion process is governed by the ratio of the oxidant to the fuel (O/R) used for combustion [15, 16, 41]. Since, citric acid is a polyhydroxy carboxylic acid with three carboxylic acid groups and one hydroxyl group and has a heat of combustion of 10.2 kJ/g, it can act both as a very good complexing agent as well as a fuel in a combustion reaction [37, 40–42]. Based on the concept of

propellant chemistry, the ratio of the oxidizing valency of the metal nitrates (O) to the reducing valency of the fuel (R), i.e., O/R should be unity to get the maximum exothermicity during a combustion reaction [15, 16, 41]. We have calculated the (O/R) ratio of the oxidant to the fuel for the systems under investigation. The oxidizing and reducing valencies were calculated by considering the valencies of elements as +4 for Ce, +4 for Zr, +3 for Al, +3 for Fe, +3 for Bi, +2 for Zn, +4 for Sn, +4 for C, +1 for H, -2 for O, and 0 for N. Thus, the oxidizing valencies for $(\text{NH}_4)_2[\text{Ce}(\text{NO}_3)_6]$ is -24, for $\text{Al}(\text{NO}_3)_3$, $\text{Fe}(\text{NO}_3)_3$, $\text{Bi}(\text{NO}_3)_3$ is -15, for $\text{SnO}(\text{NO}_3)_2$, $\text{Zn}(\text{NO}_3)_2$, $\text{ZrO}(\text{NO}_3)_2$ is -10, and the reducing valency for citric acid is +18, respectively.

For a complete combustion reaction, the oxidant and the fuel should be present in a stoichiometric ratio. Following Pederson's reaction model, the idealized combustion reaction involving the corresponding metal nitrates and citric acid may be represented as follows [40, 41]. Here, we have not taken into consideration of the water of hydration for calculation.



The calculated C/N ratio is around 0.277 for the reactions corresponding to Eqs. 1–6 and is 0.22 for Eq. 7,

i.e., the C/N ratio for which the value of O/R ratio is expected to be unity. So, we have optimized the C/N ratio to be very close to its near whole number, i.e., 0.3. For the experimentally used C/N ratio of 0.3, the ratio of the oxidizing valency of the oxidizing group to the reducing valency of the fuel (O/R) calculated is around 0.92 for Eqs. 1–6, which is closer to unity and a slightly lower value of 0.74 for Eq. 7. This indicates that the composition corresponding to Eq. 7 is comparatively a fuel rich composition and the compositions shown in Eqs. 1–6 are comparatively fuel lean compositions. It is also interesting to note the lower enthalpy changes of around -140 to -146 J/g exhibited by the C1 and F1 batches although they are having dissimilar (O/R) ratios. On the other hand, the batches A1, B1 Zn1, Zr1, F1, and Sn1 with a similar (O/R) ratio of 0.92, exhibited a different enthalpy of decomposition as well as decomposition temperatures. This emphasizes that in addition to the effect of oxidant to fuel ratio, i.e., O/R, the metal cation, its valency, charge, and oxidizing power also play a vital role in controlling the auto-combustion reaction as revealed from our experimental results.

TG/DTA of the ash powders

The ash powders derived from the different gel batches such as Sn1g, Zn1g, F1g, A1g, B1g, C1g, and Zr1g are designated in Fig. 3 as Sn1U, Zn1U, F1U, A1gU, B1U, C1U, and Zr1U, respectively. The TG curves of the corresponding ash powders in Fig. 3, show different decomposition behavior. The TG curves of the ash powders B1U, C1U, and Zn1U show almost a straight line throughout the temperature range from 273 to 1200 K indicating a negligible weight loss. The TG curves of the ash powders Zr1U, A1U, and Sn1U decomposed in two steps. The first and second weight losses observed in the regions 273–500 and 650–800 K, respectively, is attributed to the conversion of residual carbonates to metal oxides. The weight losses observed in both the steps were different for different batches depending on the characteristic nature of different metal ions. Zn1U shows an overall weight loss of only 2.56%, B1U and C1U ash powders on the other hand, exhibited a weight increase above 700 K probably indicating the non-stoichiometric nature of the precursors ($\text{MO}_{2-\delta}$, M = Ce, Bi).

X-ray diffraction analysis

The XRD analyses of the ash powders of Ce, Zn, Bi, Al, Zr, Sn, and Fe calcined at different temperatures are shown in Figs. 4, 5, and 6 respectively. The phase formation occurs at different temperatures for different systems. Iron oxide, zinc oxide, and zirconium oxide require 773 K/6 h for complete phase formation to the corresponding hematite,

wurzite ZnO , and tetragonal ZrO_2 , respectively. Similarly, tetragonal cassiterite phase of SnO_2 was formed after calcination at 873 K for 6 h. Again, a clear transition from the nano-crystalline $\gamma\text{-Al}_2\text{O}_3$ phase to the α -alumina phase could be noticed only after calcination at 1373 K for 6 h. But the most interesting feature is the X-ray diffraction patterns of the as-synthesized ceria, and bismuth oxide powder samples shown in Figs. 4 and 5, respectively, where typical diffraction peaks of CeO_2 and Bi_2O_3 are evident even in the uncalcined stage itself. The XRD peaks of both the as-synthesized and the calcined powders of CeO_2 are quite broad thus reflecting its nano-crystalline nature. It is interesting to note that a lower enthalpy change

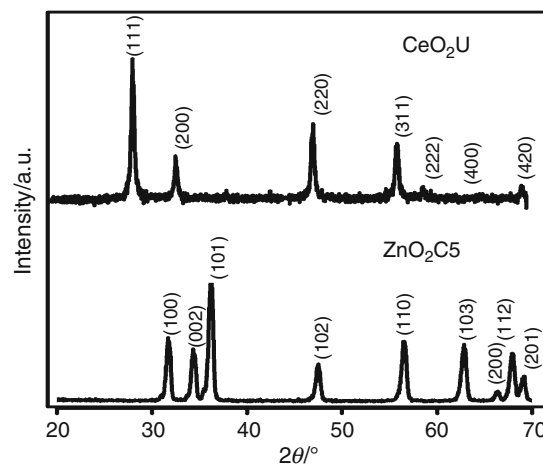


Fig. 4 XRD patterns of the calcined ash powders (CeO₂U)—uncalcined CeO₂ and (ZnO₂C5)—ZnO calcined at 773 K (500 °C)

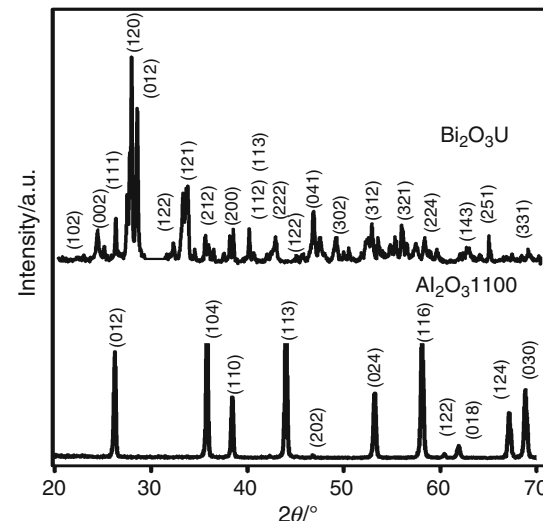


Fig. 5 XRD patterns of the calcined ash powders: (Bi₂O₃U)—uncalcined Bi₂O₃ and Al₂O₃C1100—Al₂O₃ calcined at 1373 K (1100 °C)

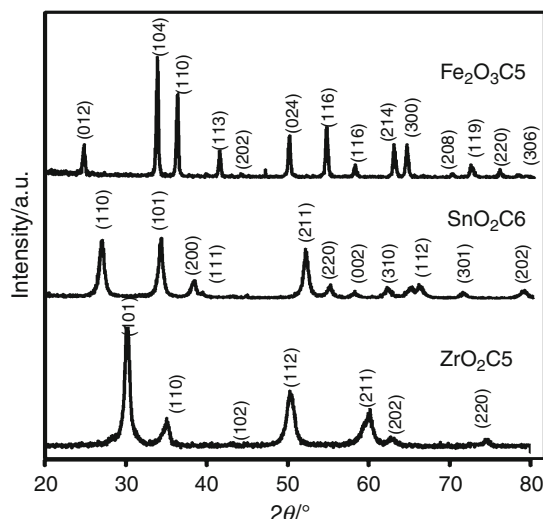


Fig. 6 XRD patterns of the calcined ash powders: $\text{Fe}_2\text{O}_3\text{C}5$ – Fe_2O_3 calcined at 773 K (500 °C), $\text{SnO}_2\text{C}6$ – SnO_2 calcined at 873 K (600 °C), and $\text{ZrO}_2\text{C}5$ – ZrO_2 calcined at 773 K (500 °C)

of -146 J/g of the combustion reaction of CeO_2 and a higher enthalpy of -348.24 J/g of Bi_2O_3 , both resulted in complete phase formation at room temperature thus emphasizing the effect of the nature of the metal ion in controlling the combustion reaction. In Fig. 7, the XRD patterns of the calcined Fe_2O_3 , SnO_2 , and ZrO_2 powder samples are shown confirming the formation of the respective oxides at 773, 873, and 773 K, respectively. From the X-ray analysis it is evident that depending on the nature of the cations, oxides such as CeO_2 and Bi_2O_3 are formed in situ during the combustion whereas oxides such as Al_2O_3 required a higher temperature of 1373 K for complete phase formation. For Bi_2O_3 , although weight loss of the gel in TG occurs between 900 and 1100 K, calcination temperature still has been fixed at 773 K for 6 h since the melting point of Bi_2O_3 is very low and is around 823 K. Moreover, the corresponding TG graphs of the Bi_2O_3 gel (Fig. 2c) and the corresponding ash powder (Fig. 3) indicates almost no weight change above 800 K. So, after careful analysis of the TG curves, calcination temperature of Bi_2O_3 has been fixed at 773 K for 6 h.

The crystallite size (D_{XRD}) of each of the metal oxide nano-particles were calculated using Scherrer's formula given by,

$$D_{\text{XRD}} = 0.9\lambda/\beta\cos\theta \quad (8)$$

where D_{XRD} is the crystallite size in nm, λ is the Cu K α radiation wavelength (0.15406 nm), β = full width at half maxima (FWHM) data in radians, and θ = X-ray diffraction angle at full maxima. The crystallite size of the powders calcined at different temperatures are presented in Table 4 which indicates that irrespective of the preparation

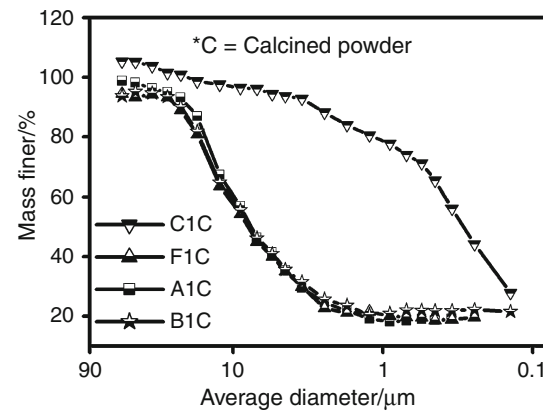


Fig. 7 Particle size distribution of the powder samples calcined at various temperatures: C1C—573 K, F1C—773 K, A1C—1373 K, and B1C—773 K

condition, all the powder samples contained crystallites in the size range of 5–18 nm.

Particle size and specific surface area

Particle size analysis of the powders calcined at different temperatures shown in Fig. 7 was carried out using a Sedigraph 5100 Micromeritics particle size analyzer and is expressed as the corresponding D_{50} values in Table 4. D_{50} is actually 50% average agglomerate size and represents the size of the secondary agglomerated clusters of 5–18 nm sized initially formed crystallites or primary particles obtained from XRD. The agglomerate size was almost two orders of magnitude higher than the primary crystallite size which is indicative of particle agglomeration. The average agglomerate size of all different metal oxide samples remained between 0.2 and 0.9 μm . In fact, the strong inter particle forces within the initially formed nano-crystalline phase powders lead to particle agglomeration.

The particle size distribution depends on the nature of ignition of the gel which in turn is related to the nature of the cations. The gel A1, B1, and F1 exhibited larger particle agglomeration whereas C1 exhibited very weak particle agglomeration with a broader distribution (Table 4). Independent of the fixed citrate to nitrate ratio of 0.3 being used here, samples from all the batches exhibited a broader particle size distribution.

The surface area of the powders calcined at different temperatures is given in Table 4. All the calcined powders have surface areas in the range of 20–58 m^2/g as shown in Table 4. The difference in surface area further indicates a strong influence of the nature of the metal ions in controlling the decomposition reaction and the powder characteristics. A large particle size (D_{BET}) calculated from surface area compared to the crystallite size measured by XRD (D_{XRD}) illustrates the rate of agglomeration among

Table 4 Physico-chemical characteristics of few representative calcined powder samples

Samples	T_C K/6 h	C_P	D_{XRD} /nm	$S_{BET}/m^2 g^{-1}$	D_{BET} /nm	D_{BET}/D_{XRD}	$D_{50}/\mu m$
CeO ₂	573	Light Yellow	12	11	75	6	0.244
Fe ₂ O ₃	773	Brown	13	55	20	2	0.826
Al ₂ O ₃	1373	White	18	20	72	4	NA
Bi ₂ O ₃	773	Yellowish Green	12	20	32	2	0.92
SnO ₂	873	White	5	58	14	3	NA

T_C calcination temperature, C_P color of the calcined powder

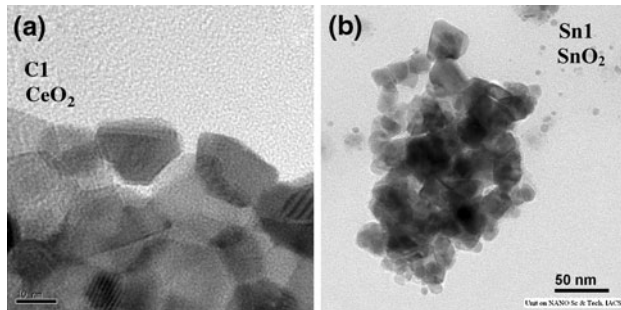


Fig. 8 **a, b** Two representative TEM pictures of the 573 K calcined ceria and 873 K calcined tin dioxide powder samples from C1 and Sn1

the particles. The relative ratio of D_{BET} and D_{XRD} , designated as the extent of agglomeration (Table 4) is smallest for powders derived from F1, B1, and S1 batches and highest for the powders derived from C1 and A1 batches.

The thermal analyses and the XRD results confirm the ease of formation of nano-crystalline metal oxide powders by the citrate–nitrate process. More importantly, the calcination temperature used for complete phase formation is quite low in all the cases compared to other methods available in the literature. Thus, in addition to maintaining a near stoichiometric citrate to nitrate ratio (CIT/NIT), the importance of the metal ion characteristics have also been established through these studies.

Transmission electron microscopy analysis

Figure 8a and b shows two representative TEM pictures of the 573 K calcined ceria (C1) and 873 K calcined tin dioxide (Sn1) powder samples. The TEM images show nano-particles of CeO₂ and SnO₂ having crystallite sizes of similar range as obtained from corresponding X-ray analysis.

Conclusions

This paper reports the synthesis and characterization of a series of nanoparticles of metal oxides by the citrate–nitrate process. We studied the effect of the metal ions on the

thermal decomposition characteristics of the corresponding gel samples. A near stoichiometric CIT/NIT ratio of 0.3 has been used for this purpose. It was found that the decomposition nature of the gel and different physical characteristics of the resultant powder samples were affected by the nature of the metal ion and the combustion reaction. It is established that nanoparticles of oxides with surface area in the range of 40–58 m²/g, crystallite size in the range of 4–18 nm with reasonably low agglomeration could be prepared by the CNP. Thus the salient features of the CNP employed here with a CIT/NIT ratio of 0.3 are as follows: (1) Nano-sized metal oxide powders could be formed even in situ during combustion. (2) Particles with high specific surface area and weaker agglomeration could be produced at lower calcination temperatures. (3) A large volume of powders could be prepared easily and safely with a low cost.

Acknowledgements The authors thank Director, Central Glass and Ceramic Research Institute for permission to publish this work. S. Banerjee acknowledges Council of Scientific and Industrial Research (CSIR) for the award of Senior Research Fellowship (SRF) during the course of this work. Technical assistance from the X-ray division of CG & CRI is acknowledged.

References

- Li Wei. Facile synthesis of monodisperse Bi₂O₃ nanoparticles. *Mater Chem Phys.* 2006;99:174.
- Jungk H-O, Feldmann C. Ployol mediated synthesis of sub-micrometer Bi₂O₃ particles. *J Mater Sci.* 2001;36:297–300.
- Liang J, Jiang X, Liu G, Deng Z, Zhuang J, Li F, Li Y. Characterization and synthesis of pure ZrO₂ nanopowders via sonochemical method. *Mater Res Bull.* 2003;38:161–8.
- Cheng H, Wu L, Ma J, Zhao Z, Qi L. Hydrothermal preparation of nanosized cubic ZrO₂ powders. *J Mater Sci Lett.* 1996;15: 895–7.
- Prasad V, Souza C-D, Yadav D, Shaikh A-J, Vigneshwaran N. Spectroscopic characterization of zinc oxide nanorods synthesized by solid-state reaction. *Spectrochim Acta A.* 2006;65:173.
- Liu B, Zeng H-C. Hydrothermal synthesis of ZnO nanorods in the diameter regime of 50 nm. *J Am Chem Soc.* 2003;125:4430–1.
- Li Y, Liao H, Qian Y. Hydrothermal synthesis of ultrafine α -Fe₂O₃ and Fe₃O₄ powders. *Mater Res Bull.* 1998;33:841–4.
- Li Y-S, Li G, Wang S-X, Gao H, Tan Z-C. Preparation and characterization of nano-ZnO flakes prepared by reactive ion exchange method. *J Therm Anal Calorim.* 2009;95:671–4.

9. Raming T-P, Winnubst A-J-A, Kats C-M-V, Philipse A-P. The synthesis and magnetic properties of nanosized hematite (α -Fe₂O₃) particles. *J Coll Interface Sci.* 2002;249:346–50.
10. He Y, Yang B, Cheng G. Controlled synthesis of CeO₂ nanoparticles from the coupling route of homogenous precipitation with microemulsion. *Mater Lett.* 2003;57:1880–4.
11. Zhang D, Fu H, Shi L, Pan C, Li Q, Chu Y, Yu W. Synthesis of CeO₂ nanorods via ultrasonication assisted by polyethylene glycol. *Inorg Chem.* 2007;46:2446–51.
12. Fraig L, Lamas D-G, Walsoe de Reca N-E. Novel method to prepare nanocrystalline SnO₂ powders by a gel-combustion process. *Nanostruct Mater.* 1999;11:311–6.
13. Bhagwat M, Shah P, Ramaswamy V. Synthesis of nanocrystalline SnO₂ powder by amorphous citrate route. *Mater Lett.* 2003;57:1604–11.
14. Yoldas B-E. Thermal stabilization of an active alumina and effect of dopants on the surface area. *J Mater Sci.* 1976;11:465–70.
15. Jain S-R, Adiga K-C, Pai Vernekar V-R. A new approach to thermochemical calculations of condensed fuel-oxidizer mixtures. *Combust Flame.* 1981;40:71–9.
16. Sousa V-C, Segadaes A-M, Morelli M-R, Kiminami RHGA. Combustion synthesized powders for varistor ceramics. *Int J Inorg Mater.* 1999;1:235–41.
17. Stefanescu M, Stoia M, Caizer C, Dippong T, Barvinschi P. Preparation of Co_xFe_{3-x}O₄ nanoparticles by thermal decomposition of some organo-metallic precursors. *J Therm Anal Calorim.* 2009;97:245–50.
18. Thomas P, Dwarkanath K, Varma K-B-R, Kutty T-R-N. Synthesis of nanoparticles of the giant dielectric material, CaCu₃Ti₄O₁₂ from a precursor route. *J Therm Anal Calorim.* 2009;95:267–72.
19. Sharma P-K, Varadan V-V, Varadan V. K. A critical role of pH in the colloidal synthesis and phase transformation of nano size α -Al₂O₃ with high surface area. *J Eur Ceram Soc.* 2003;23:659–66.
20. Waqas H, Qureshi A-H. Low temperature sintering study of nanosized Mn-Zn ferrites synthesized by sol-gel auto combustion process. *J Therm Anal Calorim.* 2010;100:529–35.
21. Lanos R, Lazău L, Păcurariu C. Metal nitrate/fuel mixture reactivity and its influence on the solution combustion synthesis of γ -LiAlO₂. *J Therm Anal Calorim.* 2009;97:209–14.
22. Prakash A-S, Khadar A-M-A, Patil K-C, Hegde M-S. Hexamethylenetetramine: a new fuel for solution combustion synthesis of complex metal oxides. *J Mater Syn Process.* 2010;10:135–41.
23. Chen Z, Yan Y. Nano-sized PDP phosphors prepared by solution combustion method. *J Mater Sci.* 2006;41:5793–6.
24. Benjaram M-R, Gunugunuri K-R, Ganesh I, Ferreira J-M-F. Single step synthesis of nanosized CeO₂–M_xO_y mixed oxides (M_xO_y = SiO₂, TiO₂, ZrO₂, and Al₂O₃) by microwave induced solution combustion synthesis: characterization and CO oxidation. *J Mater Sci.* 2009;44:2743–51.
25. Shrivakumara C, Manjunath B-B. Synthesis, structural and ferromagnetic properties of La_{1-x}K_xMnO₃ (0.0 \leq x \leq 0.25) phases by solution combustion method. *Bull Mater Sci.* 2009;32:443–9.
26. Bluthardt C, Fink C, Flick K, Hagemeyer A, Schlichter M, Volpe A Jr. Aqueous synthesis of high surface area metal oxides. *Catal Today.* 2008;137:132–43.
27. Mokkelbost T, Kaus I, Grande T, Einarsrud M-A. Combustion synthesis and characterization of nanocrystalline CeO₂-based powders. *Chem Mater.* 2004;16:5489–94.
28. Nordahl C-S, Messing G-L. Sintering of α -Al₂O₃-seeded nanocrystalline γ -Al₂O₃ powders. *J Eur Ceram Soc.* 2002;22:415–22.
29. Patil K-C, Aruna S-T, Mimani T. Combustion synthesis: an update. *Curr Opin Solid State Mater Sci.* 2002;6:507–12.
30. Devi P-S, Maiti H-S. A novel autoignited combustion process for the synthesis of Bi-Pb-Sr-Ca-Cu-O superconductors with a T_c (0) of 125 K. *J Solid State Chem.* 1994;109:35–42.
31. Chakraborty A, Devi P-S, Maiti H-S. Low temperature synthesis and some physical properties of barium-substituted lanthanum manganite (La_{1-x} Ba_xMnO₃). *J Mater Res.* 1995;10:918–25.
32. Chakraborty A, Devi P-S, Roy S, Maiti H-S. Low-temperature synthesis of ultrafine La_{0.84}Sr_{0.16}MnO₃ powder by an autoignition process. *J Mater Res.* 1994;9:986–91.
33. Basu S, Devi P-S, Maiti H-S. Nb-doped La₂Mo₂O₉: a new material with high ionic conductivity. *J Electro Chem Soc.* 2005;152:A2143–7.
34. Basu S, Chakraborty A, Devi P-S, Maiti H-S. Electrical conduction in nano-structured La_{0.9}Sr_{0.1}Al_{0.85}Co_{0.05}Mg_{0.1}O₃ perovskite oxide. *J Am Ceram Soc.* 2005;88:2110–3.
35. Kumar A, Devi P-S, Maiti H-S. Effect of metal ion concentration on synthesis and properties of La_{0.84}Sr_{0.16}MnO₃ cathode material. *J Power Sources.* 2006;161:79–86.
36. Basu S, Devi P-S, Maiti H-S. Synthesis and properties of nanocrystalline ceria powders. *J Mater Res.* 2004;19:3162–71.
37. Banerjee S, Devi P-S. Effect of citrate to nitrate ratio on the decomposition characteristics and phase formation of alumina. *J Therm Anal Calorim.* 2007;90:699–706.
38. Banerjee S, Devi P-S. Sinter-active nanocrystalline CeO₂ powder prepared by a mixed fuel process: effect of fuel on particle agglomeration. *J Nanopart Res.* 2007;9:1097.
39. Hwang C-C, Wu T-Y, Wan J, Tsai J-S. Development of a novel combustion synthesis method for synthesizing of ceramic oxide powders. *Mater Sci Eng B.* 2004;111:49.
40. Chick L-A, Pederson L-R, Maupin G-D, Bates J-L, Thomas L-E, Exarhos G-J. Glycine–nitrate combustion synthesis of oxide ceramic powders. *Mater Lett.* 1990;10:6–12.
41. Purohit R-D, Saha S, Tyagi A-K. Nanocrystalline thoria powders via glycine–nitrate combustion. *J Nucl Mater.* 2001;288:7–10.
42. Devi P-S, Rao M-S. Rare-earth chromium citrates as precursors for rare-earth chromites: lanthanum biscitratato chromium(III) dihydrate. *La[Cr(C₆H₅O₇)₂]·2H.* *Thermochim Acta.* 1989;153:181.
43. Devi P-S, Rao M-S. A comparative study on the thermal decomposition of lanthanide biscitratato chromate(III) hydrates, Ln[CrC₆(H₅O₇)₂]·nH₂O. *J Therm Anal.* 1997;48:909–16.
44. Chandradass J, Kim K-H. Effect of acidity on the citrate-nitrate combustion synthesis of alumina-zirconia composite powder. *Met Mater Inter.* 2010;15:1039–43.
45. Matraszek A, Radominska E, Szczygiel I. Modified Pechini synthesis of La, Ce, and Pr orthophosphates and characterization of obtained powders. *J Therm Anal Calorim.* 2010; doi: [10.1007/s10973-010-1063-7](https://doi.org/10.1007/s10973-010-1063-7). Online FirstTM.
46. Pinheiro da Silva M-F, de Souza Carvalho F-M, da Silva Martins T, de Abreu Fantini M-C, Isolani P-C. The role of citrate precursors on the morphology of lanthanide oxides obtained by thermal decomposition. *J Therm Anal Calorim.* 2010;99:385–90.
47. Pinheiro da Silva M-F, Soeira L-S, Daghastanli K-R-P, Martins T-S, Cuccovia I-M, Freire R-S, Isolani P-C. CeO₂-catalyzed ozonation of phenol, the role of cerium citrate as precursor of CeO₂. *J Therm Anal Calorim.* 2010;102:907–13.
48. Wyrzykowski D, Hebanowska E, Nowak-Wiczk G, Makowski M, Chmurzyński L. Thermal behaviour of citric acid and isomeric aconitic acids. *J Therm Anal Calorim.* 2010; doi: [10.1007/s10973-010-1015-2](https://doi.org/10.1007/s10973-010-1015-2). Online FirstTM.
49. Bahadur D, Rajakumar S, Kumar A. Influence of fuel ratios on auto combustion synthesis of barium ferritenano particles. *J Chem Sci.* 2006;118:15–21.
50. Purohit R-D, Tyagi A-K. Auto-ignition synthesis of nanocrystalline BaTi₄O₉ powder. *J Mater Chem.* 2002;12:312–6.
51. Lide D-R. CRC Hand book of chemistry and physics. 75th ed. USA: CRC Press; 1994. p. 1913–95.